

Evolution of the bulk electric field in capacitively coupled argon plasmas at intermediate pressures

Máté Vass^{1,2,*} , Sebastian Wilczek² , Aranka Derzsi¹ ,
Benedek Horváth¹ , Peter Hartmann¹  and Zoltán Donko¹ 

¹ Institute for Solid State Physics and Optics, Wigner Research Centre for Physics, 1121 Budapest, Konkoly-Thege Miklós str. 29-33, Hungary

² Department of Electrical Engineering and Information Science, Ruhr-University Bochum, D-44780, Bochum, Germany

E-mail: vass@aept.ruhr-uni-bochum.de

Received 8 December 2021, revised 14 March 2022

Accepted for publication 1 April 2022

Published 25 April 2022



Abstract

The physical characteristics of an argon discharge excited by a single-frequency harmonic waveform in the low-intermediate pressure regime (5–250 Pa) are investigated using particle-in-cell/Monte Carlo collisions simulations. It is found that, when the pressure is increased, a non-negligible bulk electric field develops due to the presence of a ‘passive bulk’, where a plateau of constant electron density forms. As the pressure is increased, the ionization in the bulk region decreases (due to the shrinking of the energy relaxation length of electrons accelerated within the sheaths and at the sheath edges), while the excitation rate increases (due to the increase of the bulk electric field). Using the Fourier spectrum of the discharge current, the phase shift between the current and the driving voltage waveform is calculated, which shows that the plasma gets more resistive in this regime. The phase shift and the (wavelength-integrated) intensity of the optical emission from the plasma are also obtained experimentally. The good qualitative agreement of these data with the computed characteristics verifies the simulation model. Using the Boltzmann term analysis method, we find that the bulk electric field is an Ohmic field and that the peculiar shape of the plasma density profile is partially a consequence of the spatio-temporal distribution of the ambipolar electric field.

Keywords: capacitively coupled plasmas, intermediate pressure regime, PIC/MCC simulations


(Some figures may appear in colour only in the online journal)

1. Introduction

Low temperature capacitively coupled plasmas (CCPs) are important tools for various industrial and biological applications [1–5]. These plasma sources, when operated in the

intermediate pressure range are extensively used in thin film processing, e.g. fabrication of solar panels [6–9]. Although there seems to be no strict consensus on what exact pressure interval the term ‘intermediate pressure’ stands for, in most cases it denotes the region of $p \gtrsim 100$ Pa. Due to their prevalence in industrial applications, the thorough understanding of the plasma characteristics in this pressure regime is required. Investigations in this pressure regime have been conducted concentrating on specific industrial applications (such as deposition of thin films and applications of very high frequency plasmas for materials processing) [10–14] and also on general

* Author to whom any correspondence should be addressed.

 Original content from this work may be used under the terms of the [Creative Commons Attribution 4.0 licence](https://creativecommons.org/licenses/by/4.0/). Any further distribution of this work must maintain attribution to the author(s) and the title of the work, journal citation and DOI.

plasma characteristics (such as the effect of metastable atoms and voltage waveform tailoring) [15–19]. Recently, Kawamura *et al* [20] investigated current driven discharges in the 0.2–6 Torr pressure range by 1D particle-in-cell/Monte Carlo collisions (PIC/MCC) simulation and developed the ‘passive bulk’ model to describe various aspects of the fundamental physics of argon CCPs at these pressures. They found, that as the pressure increases, the plasma develops a ‘passive bulk’, where the mean electron density profile exhibits a plateau of constant density. Ionization occurs only in the vicinity of the sheath edges, thus, the power deposition in the bulk region contributes to no ionization. This has also been shown using the electron energy probability functions (EEPFs) extracted from the simulations: whereas at low pressure the EEPF resembles a ‘two-temperature’ profile, in the intermediate pressure regime the EEPF in the discharge center resembles that of a Druyvesteyn-distribution, where there are very few electrons having energies above the ionization threshold (15.8 eV for Ar).

In this paper, we investigate the low-intermediate pressure regime of an argon CCP, paying particular attention to the electric field generated in the bulk due to the aforementioned change in the electron density profile, i.e. the occurrence of the density plateau in the intermediate pressure regime. In conventional low pressure plasma models, the electric field outside the sheath region is usually neglected, as it is very low compared to the sheath electric field [1, 4]. However, this is not completely accurate, as the ambipolar electric field has a significant impact on the electron power absorption and thus the electron dynamics of the discharge, which is situated in the vicinity of the sheath edge, but on the side of the plasma bulk [21]. Still, the electric field inside the plasma bulk, i.e. in the neighbourhood of the discharge center is, mostly justifiably, fully neglected. An exception to this is the drift-ambipolar discharge operation mode (developing typically in electronegative discharges), where the electric field inside the bulk is appreciable due to the low conductivity of the bulk plasma [22–27]. We show that the presence of the non-negligible bulk electric field in the intermediate pressure regime of electropositive discharges has far-reaching consequences on the overall discharge characteristics. Furthermore, we show that this field is an Ohmic field via the Boltzmann term analysis, which is a computational method to divide the spatio-temporal electric field and power absorption into physically different terms. This method has previously been used to investigate electron power absorption in CCPs operated at atmospheric pressure [28] and at low pressure in case of inert gases [21, 29–32], reactive gases [23, 24, 33] and in magnetized low pressure CCPs [34–36] as well. We explain the characteristics and the relation between the Ohmic and ambipolar electric fields in the intermediate pressure regime, which give rise to the peculiar ionization profile and, consequently, the ‘passive bulk’, most notably visible in the presence of the plateau in the electron density. Besides the numerical studies, we conduct experiments as well, to be able to benchmark some of the computed characteristics with

measured data. These include (i) the spatial distribution of the time-averaged wavelength-integrated optical emission of the plasma and (ii) the phase shift between the discharge voltage and current [37–39]. Both of these characteristics change with varying the pressure and provide, therefore, important checks for the simulation results.

The paper is structured as follows: in section 2, the theoretical background of the Boltzmann term analysis is briefly described, together with the specifications of the PIC/MCC simulations used in this study. In section 3, the experimental setup and measurement methods are introduced. In section 4 results are presented and discussed. Finally, in section 5, conclusions are drawn.

2. Computational method and Boltzmann term analysis

Our simulations are based on a 1d3v electrostatic PIC/MCC code [40, 41]. We study argon discharges in the pressure range between 5 and 250 Pa, for a fixed electrode gap of $L = 25$ mm. One of the electrodes (situated at $x/L = 0$) is powered by a single-frequency waveform with a voltage amplitude of $U_0 = 225$ V at a frequency of $f = 13.56$ MHz, with the other electrode (situated at $x/L = 1$) being at ground potential. A gas temperature of $T_g = 350$ K is assumed. For the electrode surface model an elastic electron reflection coefficient of 0.5 [42], and an ion induced secondary electron emission coefficient of 0.07 [43] is used. The code traces electrons and singly-charged positive argon ions. The cross sections for the electron–atom and ion–atom collisions are taken from [44, 45], respectively, and the collision models are identical to those used in e.g. [31]. A spatial resolution of $N_x = 1000$ grid points and a temporal resolution of $N_t = 15\,000$ time steps within one RF cycle are used. The superparticle number is kept at $\approx 3 \times 10^5$ in all cases. The simulations provide multiple discharge characteristics, including the electron density, the ionisation and excitation source functions, and the electron energy distribution function, which are analysed over the wide pressure range considered. The computed waveform of the discharge current is used to observe the onset of the resistive nature of the plasma with increasing pressure, as characterised by the phase angle between the current and driving voltage waveforms. To obtain high precision simulation results, averaging of the data over 4×10^3 RF cycles is conducted after reaching full convergence in each case.

Input data for the Boltzmann term analysis are also computed in the simulation code. This analysis method is based on dividing the spatio-temporally resolved electric field into physically different terms and has been thoroughly described in [21, 31, 33]. Therefore, here we only mention the most essential concepts. The method is based on the first velocity moment equation of the 1D Boltzmann equation, i.e. the electron momentum balance equation. This equation can be rearranged for the electric field, and thus divided into different terms according to $E_{\text{tot}} = E_{\text{in}} + E_{\nabla p} + E_{\text{Ohm}}$ [33], where

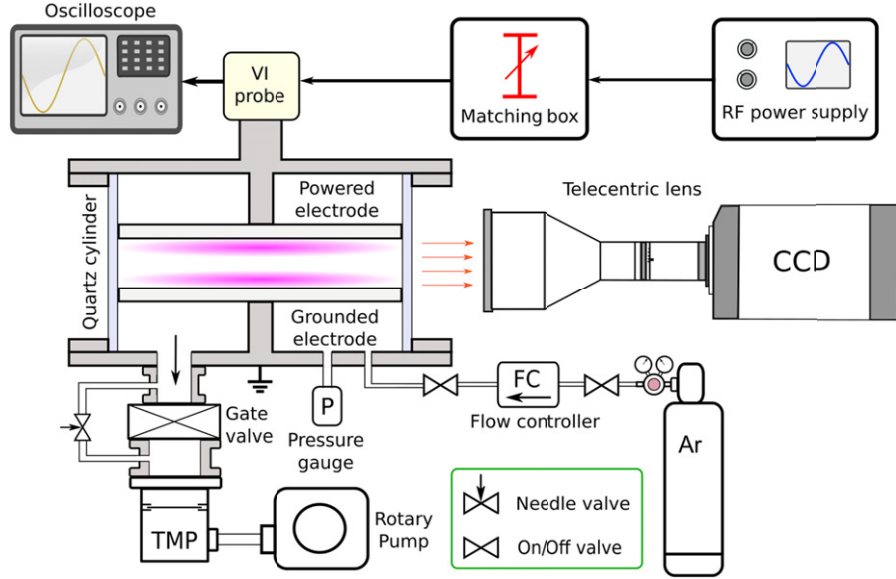


Figure 1. Scheme of the experimental setup.

$$\begin{aligned}
 E_{\text{in}} &= -\frac{m_e}{n_e e} \left[\frac{\partial}{\partial t} (n_e u_e) + \frac{\partial}{\partial x} (n_e u_e^2) \right], \\
 E_{\nabla p} &= -\frac{1}{n_e e} \frac{\partial}{\partial x} p_{\parallel}, \\
 E_{\text{Ohm}} &= -\frac{\Pi_c}{n_e e}.
 \end{aligned} \quad (1)$$

In these equations n_e and u_e are the electron density and mean velocity, respectively, m_e is the electron mass and e is the elementary charge. p_{\parallel} denotes the diagonal element of the electron pressure tensor, where ‘parallel’ refers to the direction of the discharge axis, which is perpendicular to the electrodes’ planes. Π_c incorporates the change of electron momentum due to collisions.

Each of these terms corresponds to a different physical mechanism: the inertia term, E_{in} is the electric field needed to compensate the change in the electrons’ momentum. The Ohmic field, E_{Ohm} is the consequence of collisions between electrons and particles of the background gas. $E_{\nabla p}$, the electric field corresponding to the pressure gradient [46], is usually split into two separate terms, according to $E_{\nabla p} = E_{\nabla n} + E_{\nabla T}$, where

$$\begin{aligned}
 E_{\nabla n} &= -\frac{T_{\parallel}}{n_e e} \frac{\partial n_e}{\partial x}, \\
 E_{\nabla T} &= -\frac{1}{e} \frac{\partial T_{\parallel}}{\partial x}.
 \end{aligned} \quad (2)$$

Here T_{\parallel} denotes the parallel electron temperature calculated as $T_{\parallel} = p_{\parallel}/n_e$. $E_{\nabla n}$ is, in quasineutral regions, identical to the ‘classical ambipolar’ electric field (see e.g. [22]) and $E_{\nabla T}$ originates from the gradient of the electron temperature.

3. Experimental setup and methods

The experiments are based on a geometrically symmetric CCP source (‘Budapest v.3 cell’), which was first introduced in [47]. A sketch of the system is shown in figure 1.

The stainless steel, plane-parallel and circular electrodes of the discharge are enclosed by a quartz cylinder with inner diameter of 142 mm serving as transparent dielectric wall of the discharge cell. The electrodes have identical radii of $r = 70$ mm, and the gap between them is $L = 25$ mm. The chamber can be evacuated when the gate valve is open, via a turbomolecular and a rotary pump. The base pressure of the system is approximately 10^{-5} Pa. The experiments are performed in a gas flow of $\sim 1\text{--}3$ sccm set by a flow controller. A needle valve allows fine control of the gas pressure in the chamber, which is measured by capacitive gauges (Pfeiffer Vacuum CMR264 and MKS Baratron 631A).

The upper electrode is driven by a RF waveform generator (Tokyo Hy-Power RF-150) via an impedance matching box (Tokyo Hy-Power MB-300). The lower electrode is grounded. The voltage between the electrodes and the RF current are monitored by a VI probe (Solayl Vigilant Sensor) connected to a fast oscilloscope (Tektronix DPO-4104B). The optical diagnostic tool of the setup is a CCD camera (Allied Vision GX1050), which has a bi-telecentric lens (Thorlabs MVTC23005). Using this camera, we record the spatial distribution of the time-averaged, wavelength-integrated light emission from the plasma. Due to the lateral uniformity of the plasma, the two-dimensional data are averaged in the direction perpendicular to the discharge axis, which reduces the noise significantly.

As we expect a change of the nature of the plasma impedance as a function of the gas pressure, we also record the voltage and current signals with the oscilloscope connected

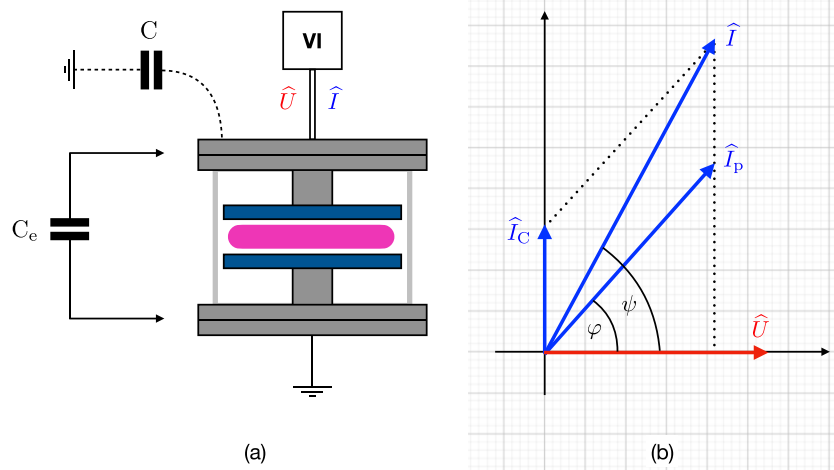


Figure 2. (a) The VI probe senses the discharge voltage (\widehat{U}), as well as the total current, (\widehat{I}) flowing in the circuit. C is the stray capacitor, C_e is an external capacitor used for calibration (see text). (b) Complex amplitudes of the discharge voltage (\widehat{U}), the plasma current (\widehat{I}_p), the current flowing through the stray capacitor (\widehat{I}_C), and the total current sensed by the VI-probe (\widehat{I}).

to the VI probe. Due to the high, 5 GSa/s sampling rate of the oscilloscope, the phase between the current and voltage signals, ψ , can be measured with an uncertainty of $\lesssim 1^\circ$. This phase is, however, not the real phase shift between the plasma current, $I_p(t)$, and the applied voltage, $U(t)$, due to the presence of a stray capacitance, C , between the powered electrode and the surrounding grounded surfaces, see figure 2(a). In order to obtain the real phase shift, this stray capacitance has to be known.

For the determination of the stray capacitance, the amplitude of the total current, I , is measured in the circuit under different conditions: three different external capacitors (C_e) with known capacitances of 23.5 pF, 34 pF and 51 pF are individually wired parallel to the electrodes, while there is no plasma in the vacuum chamber. From $I(C_e)$, the sum of the stray capacitance and the capacitance of the electrodes, $C + C_0$, can be determined. Before that, the calibration factor of the VI probe for the current measurement is determined relying on the fact that the current flowing through the external capacitor with known capacitance can be calculated from the voltage as $U2\pi fC_e$. The pair of electrodes is assumed to form an ideal plane capacitor, of which the capacitance is $C_0 = \epsilon_0 r^2 \pi / L = 5.45$ pF. Based on the above, the value of the stray capacitance is estimated to be $C = 8.21$ pF. The amplitude of the current flowing through this stray capacitance can be calculated as $I_C = U2\pi fC$; this current remains constant during the course of the measurements and we know that it leads the discharge voltage by 90° , as shown with complex amplitudes \widehat{I}_C and \widehat{U} , in figure 2(b). Based on this figure, the real phase shift between the current of the plasma and the voltage, φ , can be calculated from the measured phase shift between the total current and the voltage, ψ , as

$$\varphi = \arctan \left(\frac{I \sin \psi - I_C}{I \cos \psi} \right). \quad (3)$$

4. Results

In this section, results are presented for a voltage amplitude of $U_0 = 225$ V, a frequency of $f = 13.56$ MHz and a discharge gap of $L = 25$ mm in a pressure range between 5 Pa and 250 Pa.

Figure 3(a) shows the spatio-temporally averaged electron density, n_e (blue line), and the temporally averaged sheath width, s (red line), while panel (b) shows the spatio-temporally averaged electron power absorption, P_e as a function of the pressure. The increase of the electron density is monotonic with the pressure, but the rate of increase is slower than linear as at higher pressures the ratio of the number of ionizing collisions and the total number of collisions is smaller than at low pressures. The sheath width (computed according to equation (13) of [48]) decreases monotonically as the pressure is increased, which is in accordance with the increased density of the plasma.

A similar trend can be observed in panel (b), in case of the spatio-temporally averaged electron power absorption. The discharge current is the sum of the currents carried by the electrons and the ions, and the displacement current. The latter is dominant at the electrodes and within the sheath regions, whereas the electron current is dominant in the bulk plasma. The ion current is normally negligible as compared to these components. With the increase of the plasma density, the sheath width decreases at constant voltage, and thus the electric field at the electrodes and the displacement current ($\propto \partial E / \partial t$) increases. Due to the requirement of current continuity, this needs to be accompanied by an increase of the conduction current in the bulk. As the higher pressure results as well in higher collisionality, the conductivity of the bulk can only be maintained by an enhanced bulk electric field. These effects lead to an increased power absorption at higher pressures.

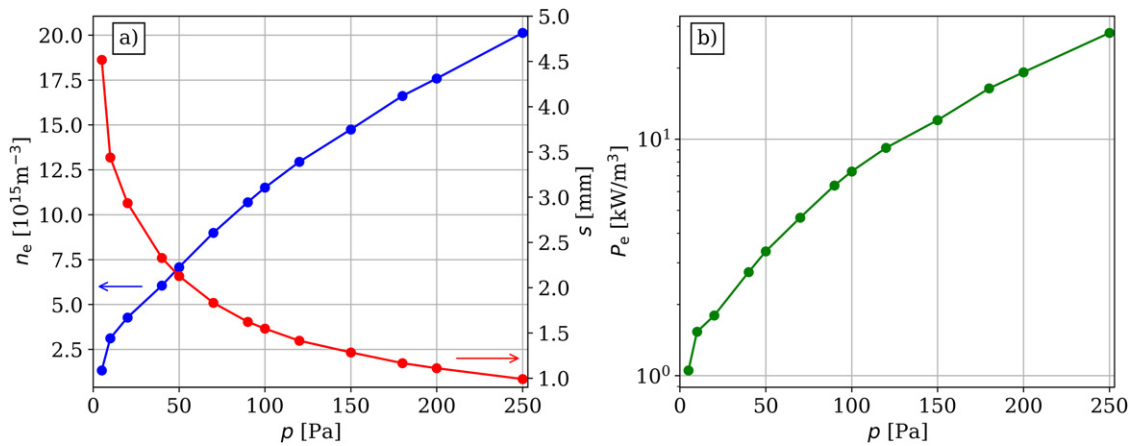


Figure 3. (a) Spatio-temporally averaged electron density, n_e , temporally averaged sheath length, s and (b) space- and time-averaged electron power absorption, P_e , as a function of pressure. Discharge conditions: $U_0 = 225$ V, $f = 13.56$ MHz, $L = 25$ mm.

In order to investigate this pressure regime in more detail, figure 4 shows the temporally averaged electron density, n_e (panel (a)), the temporal average of the ionization source function, S_{ion} (panel (b)), the temporal average of the total excitation rate, S_{exc} (panel (c)) and the total wavelength-integrated intensity, I_{int} obtained from the experiment (panel (d)) as functions of the position for four specific pressure values: 5 Pa, 50 Pa, 150 Pa and 250 Pa. As seen in panel (a), as the pressure is increased, the electron density profile changes from a ‘cosine-shape’ to a ‘passive bulk’ scenario, as reported by [20], where a high density plateau is developed in the bulk region, and a sharp increase/decrease is present only in the sheath region. This can be observed for 50 Pa and 150 Pa. At the highest pressure considered, i.e. at 250 Pa, a similar profile is observed, with the crucial difference that the density is no longer ‘flat’ in the bulk, but exhibits a small maximum in the discharge center. This behaviour of the electron density can be explained based on panel (b), i.e. the temporally averaged ionization source function, S_{ion} . At 5 Pa, most of the ionization happens in the bulk region, which is caused by electrons accelerated by the expanding sheaths (and the ambipolar electric field present there [22]), which, due to the low pressure and the correspondingly high mean free path and wide sheaths, can cause ionization over a large spatial region. As the pressure is increased, and the mean free path together with the sheath width shrinks, electrons can no longer reach the discharge center with a high energy, which decreases the ionization in the bulk. As the sheath widths decrease, the ionization maxima, which are close to the maximum sheath widths, are shifted towards the electrodes. Note that the ionization source functions exhibit an exponential decrease (showing up as straight line segments in the logarithmic-scale plot of figure 4(b)) at the bulk side from their maxima, indicating the decay of the flux of electrons accelerated to high energies upon sheath expansion. This leads to the peculiar shape of the density profile seen in panel (a) for the higher pressures: the high ionization around the sheath widths leads to the sharp increase in the density, and the lack of ionization in the bulk region, especially in case of 150 Pa, leads to the density plateau observed in panel (a). It is important to note that increasing the pressure to 250 Pa, the

ionization increases slightly in the center (see figure 4(b)) due to the increase of the bulk electric field, more precisely due to the increase of $(E/N)_{\text{bulk}}$. This leads to the change that the density profile in the bulk region is no longer flat.

Panel (c) shows the temporal average of the excitation rate, S_{exc} , calculated from the simulation. Compared to the ionization profile, the excitation shows a different behaviour as a function of pressure: while at low pressure, the excitation and ionization profiles look similar, i.e. most of these collisions happen in the bulk region, as the pressure is increased, significant excitation is present in the bulk, which monotonously increases with the pressure. This means that even though electron impact ionization is rare at higher pressures in the bulk region, excitations are prevalent, as electrons, initially accelerated in the vicinity of the instantaneous sheath edges, can have energies high enough to cause excitation within the bulk (the threshold being 11.5 eV), but not enough for ionization (with a threshold of 15.8 eV). Panel (d) shows the wavelength-integrated intensity, I_{int} obtained from experiment. When comparing these data to the computed total excitation rate, one has to bear in mind that (i) the measured data are influenced by the wavelength-dependent sensitivity of the detection system and (ii) the calculated total excitation rate does not rigorously correspond to the total emission rate, as the coupling between these could only be accounted for by a collisional-radiative model [49, 50]. We note, that another reason for the discrepancy might be the omission of certain excited and metastable species from the simulation model, as according to [17], metastable argon species change the electron dynamics in the intermediate pressure regime appreciably, which has the effect of increasing the ionization and excitation, especially near the sheaths (cf figure 2 of [17]). Therefore, we do not expect a good quantitative agreement between these two data sets. Nonetheless, we find a good qualitative agreement: the values increase monotonically at the center of the discharge (i.e. within the bulk) with increasing pressure, which is the hallmark of the increasing bulk electric field under these conditions.

To understand the trend in the ionization in figure 4(b), first one needs to investigate the energy distribution of the

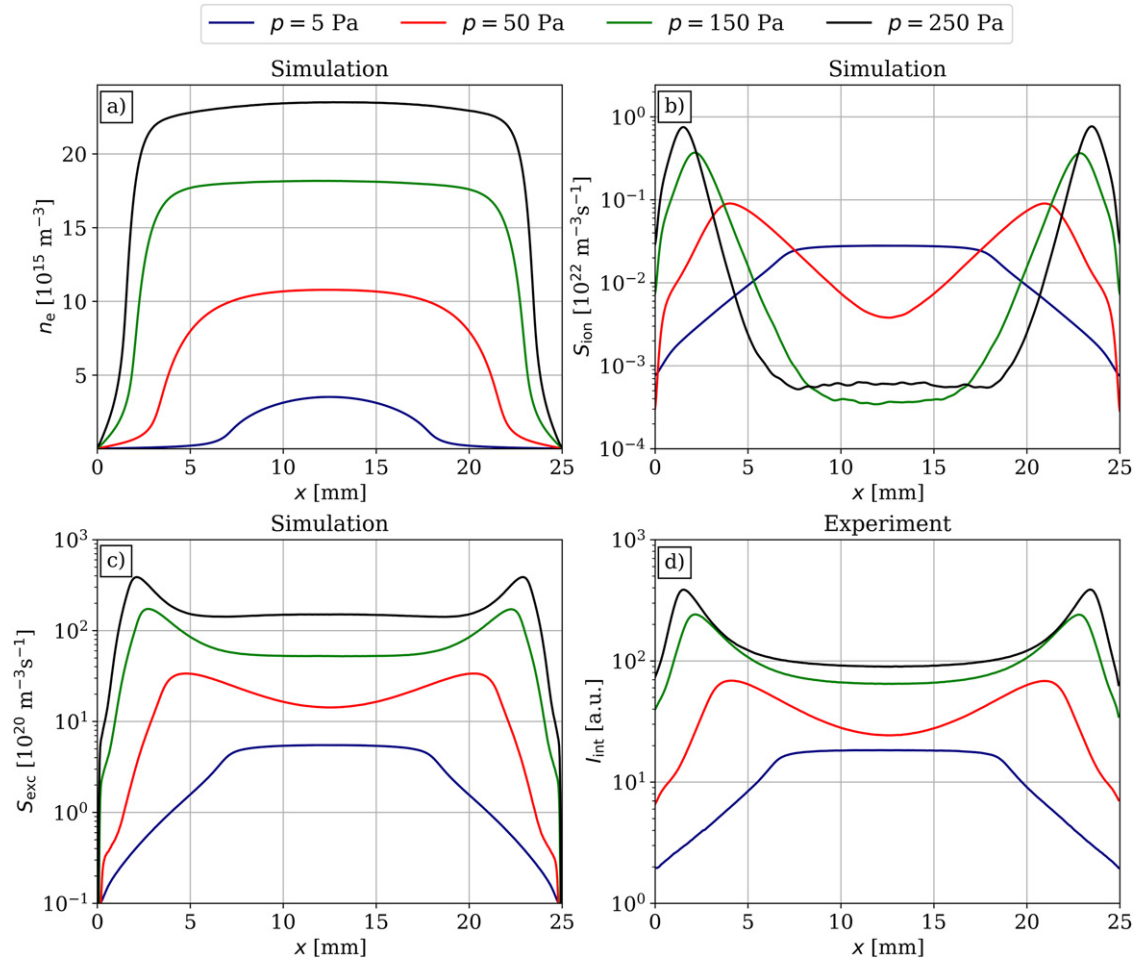


Figure 4. (a) Time-averaged electron density, n_e , (b) time-averaged ionization source function, S_{ion} , (c) time-averaged excitation rate, S_{exc} obtained from simulation and (d) total wavelength-integrated intensity, I_{int} obtained from experiment as a function of position for different pressure values. Discharge conditions: $U_0 = 225$ V, $f = 13.56$ MHz, $L = 25$ mm. The powered electrode is at $x = 0$ mm, the grounded electrode is at $x = 25$ mm.

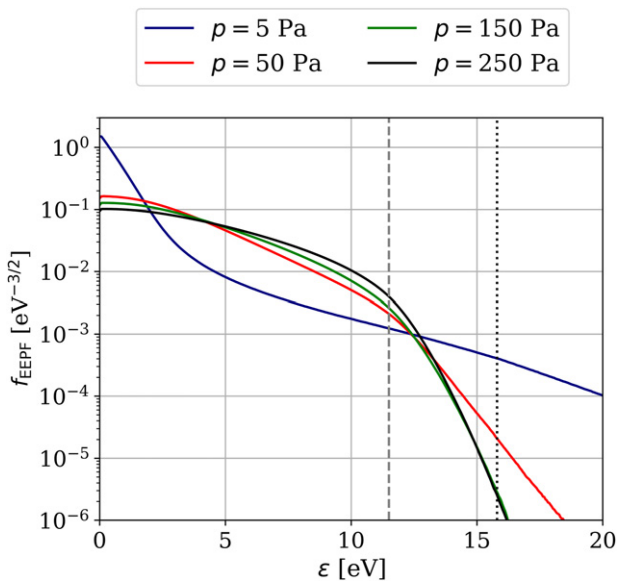


Figure 5. EEPF, f_{EPPF} in the center of the discharge obtained from the PIC/MCC simulations, for different pressure values. The dashed grey line indicates the excitation threshold of 11.5 eV considered in the simulation, together with the ionization threshold of 15.8 eV indicated by the black dotted line. Discharge conditions: $U_0 = 225$ V, $f = 13.56$ MHz, $L = 25$ mm.

electrons. Figure 5 shows the EEPF, f_{EPPF} in the center of the discharge from the PIC/MCC simulation, for the different pressures. The dashed grey and the dotted black lines indicate the energy thresholds for excitation (11.5 eV) and ionization (15.8 eV), respectively. At 5 Pa the EEPF shows a ‘two-temperature’ shape, as it is usual in low temperature single-frequency excited argon discharges [41]. There is a significant amount of high energy electrons in the center of the discharge, which leads to the high ionization in the bulk observed in figure 4(b). As the pressure is increased, the shape of the EEPF changes from a ‘two-temperature’ to a Druyvesteyn-type [20], where in the latter the high energy tail is depleted. This has the consequence of decreasing the ionization rate at this position, in accordance with figure 4(b). Furthermore, due to the fact that the EEPF increases in the intermediate energy range (5–12 eV) as the pressure is increased, the increase of S_{exc} in figure 4(c) in the discharge center as a function of pressure easily follows. The EEPFs for the two highest pressures, i.e. 150 Pa and 250 Pa, are very close to each other above 12 eV.

In order to further investigate the underlying physical mechanisms leading to the observed ionization pattern, figure 6 shows the discharge current density, j as a function of time for different pressure values (panel (a)) and its phase shift

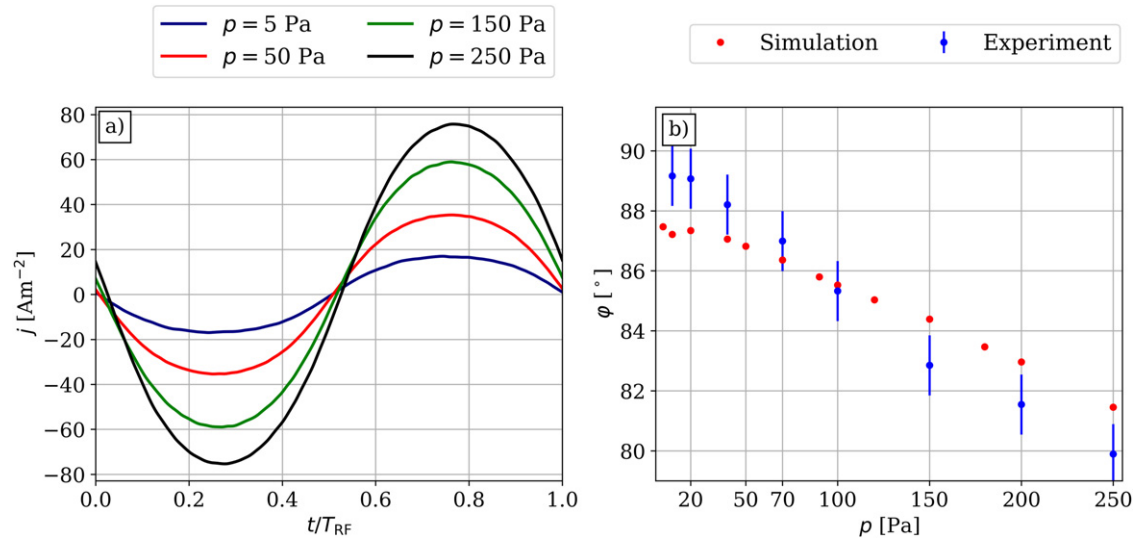


Figure 6. (a) Computed discharge current density, j over one RF cycle and (b) experimental/simulation results for its phase shift, φ (as compared to the cosine-shaped driving voltage) as a function of pressure. Discharge conditions: $U_0 = 225$ V, $f = 13.56$ MHz, $L = 25$ mm.

with respect to the cosine-shaped driving voltage waveform calculated from the simulations and obtained also from the experiment (panel (b)).

As seen in panel (a), the current amplitude is increased as a function of pressure, in accordance with the discussion provided in connection with figure 3(b). The increase of the pressure also makes the plasma more resistive, which is visible on panel (a), but is more clearly seen from the phase shift, φ in panel (b): from a value of $\approx 88^\circ$ at 5 Pa, it decreases monotonously to $\approx 82^\circ$ at 250 Pa. Thus, as the 90° phase shift would correspond to a purely capacitive discharge, the increase of the pressure shifts the plasma gradually towards the resistive regime. The corresponding experimental results for the phase shift show a good agreement with the simulation results in panel (b): the experimental results clearly confirm the monotonous shift of the discharge to a resistive regime, as the pressure of the background gas is increased. As mentioned in section 3, the experimental error is $\approx 1^\circ$. The small differences between the computed and measured values can be qualitatively understood in the following way: as the geometry of the experimental setup differs from the one dimensional geometry assumed in the simulations, physical effects, which cannot be taken into account by a 1D simulation, play a role in the experiment. These are: (i) radial losses to the walls in the experiment and (ii) a sheath being present at the walls of the experimental setup, which plays an important role in the overall discharge dynamics especially at low pressure [51]. At high pressure the first effect is important, which makes the plasma more resistive and the phase angle lower than in the simulation. At low pressures, however, the presence of the sheath at the walls becomes important, as in this case the sheath oscillation has a higher amplitude. The constructive superposition of sheath expansion at the electrode and the wall produces in the experiment more ionization as compared to a pure one dimensional system. This effect increases the conductivity and makes the discharge more capacitive at low pressures as compared to the simulation.

To further investigate the consequences of the plasma being more resistive, figure 7 shows the electric field, E (panel(a)), and the potential distribution of the plasma, Φ (panel(b)), as a function of position at the time of $t = T_{RF}/4$, i.e. at one quarter of the RF cycle. This time was chosen based on figure 6(a), as this is approximately the time when the current, and hence, the value of the electric field, is highest.

Figure 7(a) shows the consequences of the change in the pressure and the corresponding density profile on the electric field: at low pressure the electric field is low in the bulk, the main contributions come from around the sheath widths, which can be attributed to the ambipolar electric field [22]. However, the electric field in the center of the discharge can be considered negligible. This is in accordance with panel (b), where in case of 5 Pa, the potential is relatively flat in the bulk region. As the pressure is increased, however, a non-negligible, constant electric field builds up in the bulk, which extends over an increasingly wide spatial region, as the sheaths get shorter at higher pressures. This can also be observed in panel (b), where the potential increases linearly as a function of position from the powered towards the grounded electrode (at time $t = T_{RF}/4$). This slope is higher when the pressure is increased, indicating the enhanced electric field seen in panel (a). The presence of this electric field is a consequence of the resistive nature of the discharge in the intermediate pressure range. This fact can explain the marginally increased ionization in the bulk in case of 250 Pa in figure 4(b) and the corresponding local increase of the density in the center of the discharge (figure 4(a)). The value of the reduced electric field in the bulk region, $(E/N)_{\text{bulk}}$, at one quarter of the RF-cycle is ≈ 10 Td for 150 Pa, and ≈ 12 Td for 250 Pa. Although the reduced electric field is increased only by 20%, the corresponding (Townsend) ionization coefficient (although it is rather small) is increased by an order of magnitude [52]. Thus, owing to this fact, and the reduced diffusion coefficient at a higher pressure, the increased ionization observed in figure 4(b) for 250 Pa compared to 150 Pa can be explained.

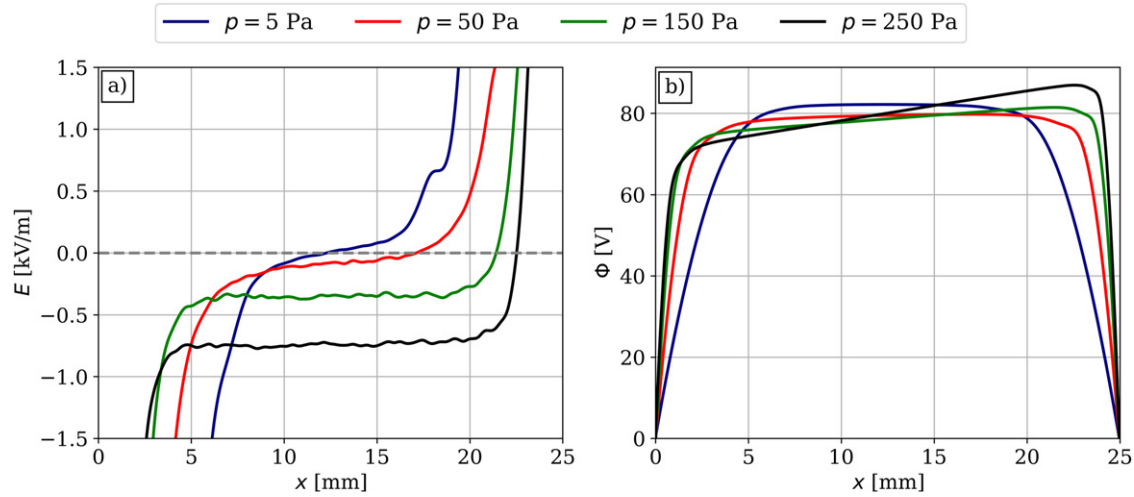


Figure 7. (a) Electric field, E , and (b) potential distribution of the plasma, Φ , as a function of position at time $t = T_{\text{RF}}/4$ for different pressure values. The values for the reduced electric field in the center of the discharge, $(E/N)_{\text{bulk}}$, are 7 Td, 10 Td and 12 Td for 50 Pa, 150 Pa and 250 Pa, respectively. Discharge conditions: $U_0 = 225$ V, $f = 13.56$ MHz, $L = 25$ mm. The powered electrode is at $x = 0$ mm, the grounded electrode is at $x = 25$ mm.

As a non-negligible bulk electric field develops due to the increasingly resistive nature of the discharge at higher pressures, because it is needed to drive the current through the ‘passive bulk’, it is reasonable to assume that this electric field is an Ohmic field, i.e. a direct consequence of collisions. (Note that the bulk Ohmic electron power absorption can be significantly enhanced even at lower pressures by increasing the driving frequency [53].)

To justify the above claim, and investigate how this effect changes with the pressure, figure 8 shows the electric field, together with the different electric field terms as calculated using the Boltzmann term analysis for four different pressure values, i.e. 5 Pa (a), 50 Pa (b), 150 Pa (c) and 250 Pa (d). In each case the inertia term is negligible. At 5 Pa (panel (a)) the Ohmic field is low in the bulk, and the electric field is almost completely determined by $E_{\nabla p}$, i.e. the pressure term, which consists of the temperature gradient term, $E_{\nabla T}$, and the ambipolar term, $E_{\nabla n}$. This fact is intimately related to the shape of the density profile at low pressure, cf figure 4(a). As there is a nonzero ionization within the bulk region, the electron density monotonously increases up to the center of the discharge, which means that the spatial gradient of the density, $\frac{\partial n_e}{\partial x}$ will have a nonzero value. As $E_{\nabla n} \propto -\frac{\partial n_e}{\partial x}$, this leads to an increase in the ambipolar electric field, as seen in figure 8(a). The ambipolar field gradually increases from a negative value (as the density increases, its negative gradient is negative), reaches zero at the density maximum, and then becomes positive (due to the monotonous decrease of the density, which creates a negative spatial gradient, making the ambipolar field positive). An opposite behaviour can be observed for the temperature gradient term, $E_{\nabla T}$. The reason for this is the spatio-temporal profile of the parallel electron temperature, T_{\parallel} . At this time of the RF cycle, the electron temperature is increased in the vicinity of the sheath at the powered electrode (i.e. at $x = 0$ mm) during its expansion, as the ambipolar field accelerates electrons thus increasing their energy and consequently, the electron temperature. Thus, there is a spatial region of high electron

temperature in the vicinity of the instantaneous sheath width. Moving away from this position towards the bulk, due to the high number of low energy electrons, the temperature sharply decreases, which leads to a negative temperature gradient and, consequently, a positive $E_{\nabla T}$. In the bulk region the spatial change of the temperature is minor, therefore $E_{\nabla T}$ is small. Moving towards the sheath edge at the opposite electrode, in the region where the electron density decreases, highly energetic electrons, that can traverse the discharge due to the low pressure, can effectively increase the temperature in the low electron density region, which leads to a positive temperature gradient and a negative $E_{\nabla T}$, as seen in panel (a).

The Ohmic field has a low value compared to the ambipolar and temperature gradient terms in the bulk region, the only contribution that is non-negligible comes from a region near the sheath edges, where the electron density decreases and, consequently, the plasma resistivity increases. Thus, at low pressure, due to the low collisionality, the pressure gradient electric field term is dominant.

As the pressure is increased to 50 Pa (panel (b)), the overall shape of the ambipolar electric field does not change, as it is directly related to the density profile (cf figure 4(a)). The only difference is, that the contribution of $E_{\nabla n}$ gets less significant inside the bulk, as the density profile starts to be flattened out, in which case the corresponding density gradient is a small number. This trend continues at higher pressures, as well, as both in case of 150 Pa (panel (c)) and 250 Pa (panel (d)) the ambipolar field is zero in the region where the density profile exhibits a plateau, and has a sharp increase/decrease at the spatial positions where the density drastically changes. This electric field is the reason why there is a peak in the ionization in figure 4(b) in the vicinity of each electrode at pressure values ≥ 50 Pa. Due to the increased collisionality (i.e. a shift to a more resistive regime) the Ohmic electric field is enhanced as the pressure is increased. It monotonously increases in magnitude, and acquires a non-negligible value starting from 50 Pa. At 150 Pa and 250 Pa, this is the electric

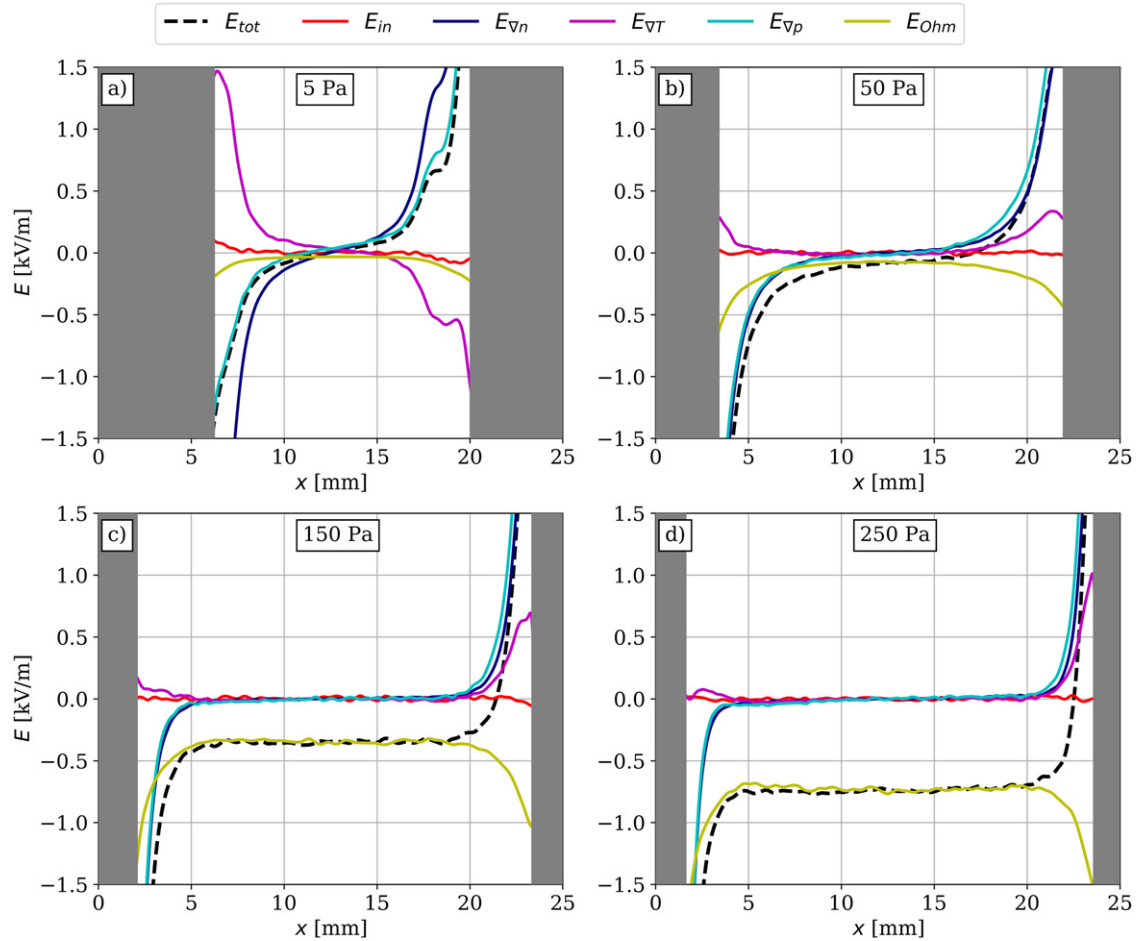


Figure 8. Electric field terms at time $t = T_{RF}/4$ for different pressure values. The shaded region masks the sheath region, where the signal to noise ratio is too low. Discharge conditions: $U_0 = 225$ V, $f = 13.56$ MHz, $L = 25$ mm. The powered electrode is at $x = 0$ mm, the grounded electrode is at $x = 25$ mm.

field term that dominates in the bulk region, thus, in accordance with the findings and the corresponding hypothesis presented above, it is indeed the Ohmic electric field that constitutes the non-negligible electric field within the bulk. As the plasma gets more resistive due to the increase of the pressure and the corresponding increase of the current density, the Ohmic electric field, whose purpose is to drive this increased current through the discharge, increases accordingly. This also explains why the temperature gradient electric field term exhibits a different behaviour at higher pressures (i.e. ≥ 50 Pa) as compared to the low pressure case: in the vicinity of the sheath edge near the powered electrode, $E_{\nabla T}$ decreases, and becomes negligible above 150 Pa. On the other hand, near the grounded electrode, this electric field is increased, i.e. from an initially negative value at low pressure, it acquires a positive value which monotonously increases as a function of pressure. The reason for this trend lies in the spatio-temporal distribution of the electron temperature, which is greatly affected by the presence of the bulk electric field: although during sheath expansion, electrons are accelerated and T_{\parallel} increases, due to the presence of the bulk electric field, the overall temperature of bulk electrons increases, and thus the temperature gradient will be less severe than at low pressures. This is why $E_{\nabla T}$ is decreased in the vicinity of the powered electrode. The same

reasoning can be applied for the increased value of this electric field at the grounded electrode: electrons are accelerated by the Ohmic electric field inside the bulk at high pressure, leading to an increased temperature in this spatial region. This electric field is high whenever the density is nearly constant. As the density drops, the Ohmic electric field decreases due to the lower electron density, but the ambipolar field increases at a fast rate (cf panel (d)): the total electric field is positive near the sheath at $x \approx 24$ mm, i.e. electrons are decelerated. Thus, from an initially high temperature region inside the bulk, the temperature drops as electrons lose energy; this leads to a negative temperature gradient and a correspondingly positive value for $E_{\nabla T}$: as seen from panels (b)–(d), this effect gets more and more prominent with the increase of the pressure, the reason being the higher Ohmic (bulk) electric field and the higher electron temperature in the bulk region as its consequence.

5. Conclusions

The plasma characteristics of an argon discharge excited by a single-frequency waveform of $U_0 = 225$ V amplitude and $f = 13.56$ MHz frequency were investigated in the low-intermediate pressure regime between 5 Pa and 250 Pa, using 1d3v PIC/MCC simulations.

We have found that with increasing pressure the plasma density profile started to develop a ‘resistive bulk’, where after a sharp increase near the sheath edges a plateau with a constant density is developed. Above a given pressure value, however, the density in the discharge center started to grow again. This was also confirmed by the temporally averaged ionization source function, which exhibits a maximum inside the bulk at low pressure, but transforms into a profile having two distinct maxima at either electrodes as the pressure is increased. Similarly, the ionization decreased in the discharge center as a function of pressure up to a certain value, but then started to increase again, in accordance with the trend observed in case of the density. Furthermore, our experimental studies have confirmed the characteristic changes of the spatial distribution of the time-averaged light emission intensity from the discharge. At low pressures, the emission was found to have a wide flat part at the center of the plasma, while the increasing pressure resulted in the development of a hole in the center due to the decreasing sheath length and higher collisionality. The increasing pressure, nonetheless, resulted in an increasing intensity at the center due to the enhanced bulk electric field. Similar changes were also seen in the simulation results obtained for the total excitation rate.

Characteristic changes were also observed in the EEPF in the discharge center, which exhibited a two-temperature profile at low pressure and a Druyvesteyn-like shape in the intermediate pressure range. Due to the presence of the bulk electric field, the intermediate energy part (i.e. between 5 eV and 13 eV) increased, thus leading to a higher excitation at a higher pressure. The marginally increased ionization at 250 Pa with respect to 150 Pa can be explained by the increased bulk electric field, and the correspondingly higher reduced electric field, E/N within the bulk.

To confirm that the discharge gradually moves towards a more resistive regime as the pressure is increased, the phase shift of the current density with respect to the cosine-shaped voltage amplitude has been calculated using the Fourier spectrum of the current density, and has also been obtained from experiment. Both data sets indicated a decay of this phase from nearly 90° at the lowest pressures to $\varphi \approx 81^\circ$ at $p = 250$ Pa, thus confirming the increasing resistivity of the bulk plasma. In order to justify the claim that the bulk electric field is developed in order to drive the increased current through the discharge, thus constituting an Ohmic electric field, the Boltzmann term method has been applied to study the electric field profile at a certain time instance in the RF cycle. It was found that the bulk electric field, which increases as a function of pressure, is indeed an Ohmic electric field. This had consequences on the other electric field terms, i.e. the ambipolar and the temperature gradient terms: the former was found to be practically negligible within the bulk due to the presence of the density plateau, while the latter changed drastically near the electrodes due to the presence of the bulk electric field and the corresponding increase of the electron temperature in the bulk region. Thus, it became negligible in the region of sheath expansion, and increased during sheath collapse. Therefore, the overall simulation and experimental find-

ings clearly confirm that in the intermediate pressure regime a non-negligible electric field develops in the bulk, which has far-reaching consequences on the discharge characteristics.

Acknowledgments

This work was supported by the National Office for Research, Development and Innovation (NKFIH) of Hungary via the Grants K-134462 and FK-128924 and by the German Research Foundation in the frame of the projects ‘Electron heating in capacitive RF plasmas based on moments of the Boltzmann equation: from fundamental understanding to knowledge based process control’ (No. 428942393) and SFB 1316, project A4.

Data availability statement

The data that support the findings of this study are available upon reasonable request from the authors.

ORCID iDs

Máté Vass  <https://orcid.org/0000-0001-9865-4982>
 Sebastian Wilczek  <https://orcid.org/0000-0003-0583-4613>
 Aranka Derzsi  <https://orcid.org/0000-0002-8005-5348>
 Benedek Horváth  <https://orcid.org/0000-0002-2371-2444>
 Peter Hartmann  <https://orcid.org/0000-0003-3572-1310>
 Zoltán Donkó  <https://orcid.org/0000-0003-1369-6150>

References

- [1] Lieberman M A and Lichtenberg A J 2005 *Principles of Plasma Discharges and Materials Processing* 2nd edn (New York: Wiley)
- [2] Makabe T and Petrović Z L 2006 *Plasma Electronics: Applications in Microelectronic Device Fabrication* (Boca Raton, FL: CRC Press)
- [3] Fridman A A and Friedman G G 2013 *Plasma Medicine* (New York: Wiley)
- [4] Chabert P and Braithwaite N 2011 *Physics of Radio-Frequency Plasmas* (Cambridge: Cambridge University Press)
- [5] Fridman A 2008 *Plasma Chemistry* (Cambridge: Cambridge University Press)
- [6] Crose M, Sang-Il Kwon J, Nayhouse M, Ni D and Christofides P D 2015 *Chem. Eng. Sci.* **136** 50–61
- [7] Terakawa A 2013 *Sol. Energy Mater. Sol. Cells* **119** 204–8
- [8] Fang M, Zhang C and Chen Q 2016 *Appl. Surf. Sci.* **385** 28–33
- [9] Guo Y, Ong T M B, Levchenko I and Xu S 2018 *Appl. Surf. Sci.* **427** 486–93
- [10] Kim H J and Lee H J 2017 *Plasma Sources Sci. Technol.* **26** 085003
- [11] Kim J S, Hur M Y, Kim C H, Kim H J and Lee H J 2018 *J. Phys. D: Appl. Phys.* **51** 104004
- [12] Park H and Kim H J 2021 *Coatings* **11** 1041
- [13] Kim H J and Lee H J 2018 *J. Appl. Phys.* **123** 113302
- [14] Nunomura S and Kondo M 2007 *J. Appl. Phys.* **102** 093306
- [15] Makabe T 2019 *Japan. J. Appl. Phys.* **58** 110101
- [16] Doyle S J, Gibson A R, Boswell R W, Charles C and Dedrick J P 2020 *Plasma Sources Sci. Technol.* **29** 124002

- [17] Wen D-Q, Krek J, Gudmundsson J T, Kawamura E, Lieberman M A and Verboncoeur J P 2021 *Plasma Sources Sci. Technol.* **30** 105009
- [18] Doyle S J, Gibson A R, Boswell R W, Charles C and Dedrick J P 2019 *Phys. Plasmas* **26** 073519
- [19] Lafleur T and Chabert P 2015 *Plasma Sources Sci. Technol.* **24** 025017
- [20] Kawamura E, Lieberman M A, Lichtenberg A J and Chabert P 2020 *J. Vac. Sci. Technol. A* **38** 023003
- [21] Schulze J, Donkó Z, Lafleur T, Wilczek S and Brinkmann R P 2018 *Plasma Sources Sci. Technol.* **27** 055010
- [22] Schulze J, Derzsi A, Dittmann K, Hemke T, Meichsner J and Donkó Z 2011 *Phys. Rev. Lett.* **107** 275001
- [23] Gudmundsson J T and Snorrason D I 2017 *J. Appl. Phys.* **122** 193302
- [24] Proto A and Gudmundsson J T 2021 *Plasma Sources Sci. Technol.* **30** 065009
- [25] Liu G-H, Liu Y-X, Wen D-Q and Wang Y-N 2015 *Plasma Sources Sci. Technol.* **24** 034006
- [26] Proshina O V, Rakhimova T V, Rakhimov A T and Voloshin D G 2010 *Plasma Sources Sci. Technol.* **19** 065013
- [27] Liu G-H, Liu Y-X, Bai L-S, Zhao K and Wang Y-N 2018 *Phys. Plasmas* **25** 023515
- [28] Vass M, Wilczek S, Schulze J and Donkó Z 2021 *Plasma Sources Sci. Technol.* **30** 105010
- [29] Surendra M and Dalvie M 1993 *Phys. Rev. E* **48** 3914
- [30] Lafleur T, Chabert P and Booth J P 2014 *Plasma Sources Sci. Technol.* **23** 035010
- [31] Vass M, Wilczek S, Lafleur T, Brinkmann R P, Donkó Z and Schulze J 2020 *Plasma Sources Sci. Technol.* **29** 085014
- [32] Wilczek S, Schulze J, Brinkmann R P, Donkó Z, Trieschmann J and Mussenbrock T 2020 *J. Appl. Phys.* **127** 181101
- [33] Vass M, Wilczek S, Lafleur T, Brinkmann R P, Donkó Z and Schulze J 2020 *Plasma Sources Sci. Technol.* **29** 025019
- [34] Wang L, Wen D-Q, Hartmann P, Donkó Z, Derzsi A, Wang X-F, Song Y-H, Wang Y-N and Schulze J 2020 *Plasma Sources Sci. Technol.* **29** 105004
- [35] Zheng B, Wang K, Grotjohn T, Schuelke T and Fan Q H 2019 *Plasma Sources Sci. Technol.* **28** 09LT03
- [36] Zheng B, Fu Y, Wang K, Schuelke T and Fan Q H 2021 *Plasma Sources Sci. Technol.* **30** 035019
- [37] Harvey C, Vandenburg S and Ellingboe A R 2021 *Curr. Appl. Phys.* **28** 45–51
- [38] Huo W G, Zhang H and Ding Z F 2015 *Rev. Sci. Instrum.* **86** 023508
- [39] Liu Y-X, Wang X-Y, Zhang Q-Z, Donkó Z, Zhao K, Schulze J and Wang Y-N 2020 *Plasma Sources Sci. Technol.* **29** 12LT03
- [40] Donkó Z 2011 *Plasma Sources Sci. Technol.* **20** 024001
- [41] Donkó Z, Derzsi A, Vass M, Horváth B, Wilczek S, Hartmann B and Hartmann P 2021 *Plasma Sources Sci. Technol.* **30** 095017
- [42] Donkó Z, Hartmann P, Korolov I, Jeges V, Bošnjaković D and Dujko S 2019 *Plasma Sources Sci. Technol.* **28** 095007
- [43] Schulenberg D A, Korolov I, Donkó Z, Derzsi A and Schulze J 2021 *Plasma Sources Sci. Technol.* **30** 105003
- [44] Phelps A V and Petrovic Z L 1999 *Plasma Sources Sci. Technol.* **8** R21
- [45] Phelps A V 1994 *J. Appl. Phys.* **76** 747–53
- [46] Lafleur T and Chabert P 2015 *Plasma Sources Sci. Technol.* **24** 044002
- [47] Horváth B, Derzsi A, Schulze J, Korolov I, Hartmann P and Donkó Z 2020 *Plasma Sources Sci. Technol.* **29** 055002
- [48] Brinkmann R P 2007 *J. Appl. Phys.* **102** 093303
- [49] Vlcek J 1989 *J. Phys. D: Appl. Phys.* **22** 623
- [50] de Vries N, Iordanova E I, Hartgers A, van Veldhuizen E M, van den Donker M J and van der Mullen J J A M 2006 *J. Phys. D: Appl. Phys.* **39** 4194
- [51] Wang L, Hartmann P, Donkó Z, Song Y-H and Schulze J 2021 *Plasma Sources Sci. Technol.* **30** 054001
- [52] Hagelaar G J M and Pitchford L C 2005 *Plasma Sources Sci. Technol.* **14** 722
- [53] Zhao K, Liu Y, Zhang Q, Economou D J and Wang Y 2021 *Plasma Sci. Technol.* **23** 115404